Results in Physics 8 (2018) 805–818

Contents lists available at ScienceDirect

Results in Physics

journal homepage: www.journals.elsevier.com/results-in-physics

# Design and multi-physics optimization of rotary MRF brakes

Okan Topcu [a,*], Yiğit Taşcıoğlu [a], Erhan İlhan Konukseven [b]

[a] TOBB ETU, Sogutozu Caddesi No: 43, Sogutozu, Ankara 06560, Turkey
[b] METU, Universiteler Mahallesi, Dumlupinar Bulvari No: 1 Cankaya, Ankara 06800, Turkey

ARTICLE INFO

*Article history:*
Received 22 September 2017
Received in revised form 8 December 2017
Accepted 3 January 2018
Available online 11 January 2018

*Keywords:*
Particle swarm optimization (PSO)
Multi-physics optimization problem
Rotary MRF brake
Heat transfer
Finite element

ABSTRACT

Particle swarm optimization (PSO) is a popular method to solve the optimization problems. However, calculations for each particle will be excessive when the number of particles and complexity of the problem increases. As a result, the execution speed will be too slow to achieve the optimized solution. Thus, this paper proposes an automated design and optimization method for rotary MRF brakes and similar multi-physics problems. A modified PSO algorithm is developed for solving multi-physics engineering optimization problems. The difference between the proposed method and the conventional PSO is to split up the original single population into several subpopulations according to the division of labor. The distribution of tasks and the transfer of information to the next party have been inspired by behaviors of a hunting party. Simulation results show that the proposed modified PSO algorithm can overcome the problem of heavy computational burden of multi-physics problems while improving the accuracy. Wire type, MR fluid type, magnetic core material, and ideal current inputs have been determined by the optimization process. To the best of the authors' knowledge, this multi-physics approach is novel for optimizing rotary MRF brakes and the developed PSO algorithm is capable of solving other multi-physics engineering optimization problems. The proposed method has showed both better performance compared to the conventional PSO and also has provided small, lightweight, high impedance rotary MRF brake designs.



## Introduction

Particle swarm optimization (PSO) algorithm has become a popular tool in the field of engineering optimization in recent years [1–3]. It was first presented in 1995 by Kennedy and Eberhart [4] and it has taken its place as a simple and powerful optimal algorithm among other evolutionary algorithms. The ability to integrate it into software, its mathematical simplicity and the ease of updating the used formulas are among the forefront advantages of the PSO.

PSO algorithms are population-based metaheuristic algorithms which are inspired by the nature. PSO has its roots in computer animation technology and image rendering. The particle system of Reeves [5] was later improved by Reynolds [6] with the notion of inter-object communication which rendered individual particles capable of following some basic flocking rules. Afterwards Kennedy and Eberhart [4] made optimization capabilities of a flock of birds utilizable. PSO algorithm is designed to simulate the social behavior of fishes schooling and birds flocking. Algorithm starts with a randomly distributed set of particles (potential solutions), and then tries to increase a quality measure (fitness/cost function) by displacing particles. The particle displacement is made possible by utilizing a set of simple mathematical expressions which model some interparticle communications.

This study proposes a modified version of PSO algorithm with multiple subswarms for the multi-physics design optimization of four rotary Magneto-rheological fluid (MRF) brakes. The multi-physics design approach was made to aid geometric design, taking into consideration electromagnetism, non-Newtonian flow behavior of MRF, and heat transfer. The multi-physics model was also used to predict the steady-state thermal characteristics of coil, MRF, stator and rotor.

This paper is organized as follows. Section "The effect of subswarm" reveals the effect of subswarms based on the related works. Section "MRF devices" and Section "Haptic MRF devices" respectively provide brief introductions to MRF devices and Haptic MRF devices. Section "Multi-physics optimization" gives details about weight optimization, ampacity, ohmic heating, magnetic circuit, friction torque, and passive resistive torque required for multi-physics optimization. Section "Modified PSO algorithm" explains the proposed modified PSO algorithm for multi-physics optimization problem. Section "Multi-objective Multi-physics

* Corresponding author.
*E-mail address:* otopcu@etu.edu.tr (O. Topcu).

https://doi.org/10.1016/j.rinp.2018.01.007
2211-3797/

engineering design optimization problem" discusses rotary MRF Brakes' base designs with equality and inequality constraints. Finally Section "Results" demonstrates the experimental study, where the performance of the algorithm is compared to a common PSO.

## The effect of subswarm

It is well known that most of the multimodal function optimization problems have several variables. Furthermore, multiple global or/and local optimal solutions, and not a single optimum is common among such functions. To solve this kind of optimization problems, approaches based on evolutionary algorithms have been developed. In the evolutionary algorithms, the concept of subpopulation (or named as subswarm) is utilized especially for solving multimodal function optimization problems and multiobjective optimization problems [7].

Some innovative approaches like glowworm swarm optimization [8] and gravitational search algorithm [9] were used to find multiple solutions in multimodal problems by creating subswarms during optimization process. The two-layer particle swarm optimizations (TLPSO) is a subswarm configuration in which whole swarm divides into two and switch roles during optimization. TLPSOs [10,11] were proposed to avoid the disadvantage of trapping at a local optimum by increasing the diversity of particles. In another study multiple subswarms, which focus on locating multiple optima, was proposed [12]. In order to find as many local optima as possible typical niching methods are used. Different from typical niching methods, Otani et al. [13] made individual particles capable of leaving their current search spaces. These particles can be classified as a subswarm which is capable of re-entering the search space at any coordinates. Re-entering the search space is known as particle regeneration and it helps the subswarm to escape from local optima [14]. It is also possible to made subswarms to compete or cooperate to exploit the complementary diversity preservation mechanisms [15].

In some cases, it is best practice to shrink the population of the swarm [16]. A smaller swarm will spend less computational power by simply removing stable particles and storing their best positions [17]. All removed particles near the same local optima also represent a subswarm.

## MRF devices

MRF devices are known as passive actuators. The formations of columnar structures of the solid particles in the MRF under a magnetic field enhances the viscosity of the fluid. This strong, rapid and reversible effect was first identified by Rabinow [18] in the late 1940 s. Much of the research on MRF devices uses fluids supplied by Lord Company. [19]. Devices that operate with MRF are often classified according to mode of operation [20]. These operating modes are shear mode, valve or flow mode, squeeze mode, and magnetic gradient pinch mode. A schematic representation of these modes is given in Fig. 1. MRF devices are MRF brake, MRF damper, MRF clutch. MRF devices are used in automotive clutches, brakes for exercise equipment, seat dampeners, knee prosthesis, actuator systems, and shock absorbers.

The word haptic is derived from haptesthai, a verb belonging to ancient Greeks. Haptics focuses on simulation of the forces or torques of virtual or real physical systems. The force value is given as 6 N for the middle finger and 4.5 N for the ring finger [21]. Given the pressing forces that fingers can generate during grip, it appears that the forces produced by small MRF devices can be utilized as haptic interfaces. MRF devices are often assessed in terms of power consumption, size, and the highest response torques or forces they can provide [22–24].

## Haptic MRF devices

Haptic devices are controlled by impedance and admittance control methods [25]. In order for these control systems to be successful, the actuators that must be present at the haptic interfaces must be small, lightweight, and high impedance. In order to obtain the ideal actuator, the weight must be minimized. When the rotary MRF devices are compared with the operating modes, it is seen that the dimensional parameters of the device have great influence on the response torque. On the other hand, if these parameters are enlarged, heavy devices with high reaction torque, which are not preferred in haptic systems, will be obtained [26].

As one of the well-known passive actuators, the rotary MRF brakes have simple designs. Oppositely, optimizing the design for haptic systems is not a simple process. Transparency can be summarized as the fact that the virtual or distant environment in haptic interface feels indistinguishable from the real environment. Transparency, in other words, is used to describe small, lightweight and high impedance haptic systems [27]. The MRF brake as a passive actuator, which must be present in the haptic interfaces, must be transparent in order for the device to be successfully controlled. This paper aims to develop four different rotating MRF brake designs with lightweight, low power consumption, and high response torque for haptic applications via an improved PSO algorithm.

## Multi-physics optimization

### *Weight optimization*

In order to obtain the ideal passive actuator, it is necessary to optimize ampacity, weight, magnetic circuit, and resistive torque by changing geometric parameters. In addition to the MRF torque or force optimization, weight optimization is a new issue [24,28–31]. Lightweight actuators are both needed and essential components for many force feedback systems. The following approximate weight expression is used when calculating the weights of MRF devices.

$$m = V_{pM}\rho_{pM} + V_{MRF}\rho_{MRF} + V_{St}\rho_{St} + V_c\rho_c \quad (1)$$

In the equation, $V_{pM}$, $V_{MRF}$, $V_{St}$, and $V_c$ respectively represent volumes of the non-magnetic material, MRF, magnetic core, and wire winding. The volumes are multiplied by the densities of the

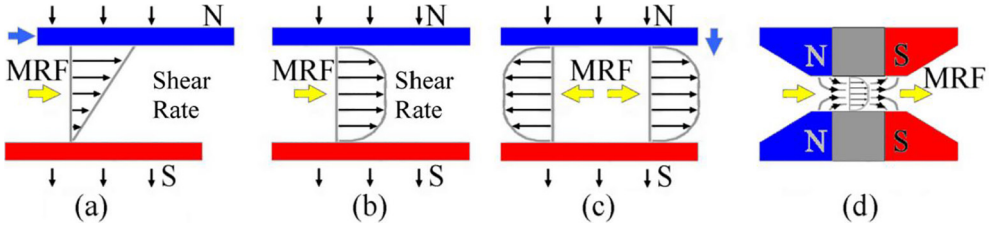


**Fig. 1.** MRF operating modes (a) shear mode, (b) flow mode, (c) squeeze mode, and (d) magnetic gradient pinch mode.

non-magnetic (paramagnetic) material, MRF, magnetic core (ferromagnetic) material and copper ($\rho_{pM}$, $\rho_{MRF}$, $\rho_{St}$ and $\rho_c$) in order to calculate the weight of the device.

*Ampacity*

In addition to weight optimization, magnetic circuit optimization must also be performed. Magnetic circuit optimization can help us obtain the material types (MRF included) to be used in production, the reaction torques to be produced and the highest current (ampacity) to be given to the magnetic circuit.

The highest current value that the conductor can withstand instantly or for a long time without causing damage is the permissible current intensity for that conductor. The highest applicable current value and application period are different from the permitted current magnitude and should be considered separately. Conductive materials such as copper and aluminum can transmit high currents without being damaged. Generally, the insulation material is damaged by not being able to withstand high temperatures. When designing an electrical circuit, one should pay attention to the system components that are affected by temperature due to current flow and resistive loss [32,33]. The permissible current intensity for conductors depends on the temperature that the insulation material can withstand, the electrical resistance of the conductor, the frequency of the current in the case of an alternating current, the conductor geometry, the ability of surrounding elements to emit heat, and the ambient temperature. If the ambient temperature is lower than the conductor temperature and the surface area of the conductor is sufficiently large, it may be expected that the permissible current value is higher than the reference value.

In short, the maximum permissible continuous current value for conductors will vary depending on the physical and electrical properties of the conductor and the type of insulation material, ambient temperature, and thermal conductivity coefficients. Depending on the insulation material used in the conductors, the maximum permissible conductor surface temperatures are typically 90 °C, 130 °C, 155 °C, 180 °C and 220 °C. When referring to the permissible current values, the conductive wires are referred to as a single wire and when the ambient temperature is at room temperature. If the wires are used in a closed environment and as part of a winding, the current values to be used as references will become approximate values.

Furthermore, high temperatures will have negative effects on the MRF [34]. Existing MRFs have typical operating temperature ranging from −40 to 150 °C. Increase in temperature of the MRF will bring about several adverse effects on the breaking torque [35]. The heat dissipation for MR brakes is a "hot" problem to be solved. Weiss et al. [36] and Liao [37] found that performance of MRF devices are unfavorably affected by the temperature increase. MRF brakes are generally limited to relatively small-power applications due to the limited cooling capacity. Hence, the current must be limited to prevent overheating of the device and the most efficient wire size must be determined. Sohn et al. [38] concluded that the steady temperature of the MRF brake should be less than 120 °C. Unlike other MRF devices in which the heat is a result of slip and friction, the heat is produced as a result of electrical energy input in MRF brakes used as haptic interface actuators [39].

*Ohmic heating*

Most of the energy losses in electric motors and electromagnets are due to resistive losses (ohmic heating) in current carrying conductors. It is important to determine the resistance of the coil (s) in order for the losses to be detected. The electrical resistance of the conductive material can be obtained in terms of the cross-sectional area through which the current flows. Electrical resistance of the conductive material is given in Eq. (2), where the proportionality coefficient $\rho_{ref}$ is represented by the electrical resistivity.

$$R_{ref} = \rho_{ref}\left(\frac{L_{ref}}{A_{ref}}\right) \tag{2}$$

The subscript "ref" is used to represent the reference temperature which represents a value due to the electrical resistance temperature of the conductor. If the operating temperatures of motors and electromagnets do not have a special cooling system in their bodies, the working temperature of the conductors used in the windings will be different from the room temperature. In this case it is necessary to calculate the new value due to the electrical resistance temperature. In conditions where the temperature difference is not too high, Eq. (3) below can be used to calculate the electrical resistance value [40].

$$R_{wire} = R_{ref}\left[1 + \alpha_{ref}(T_{wire} - T_{ref})\right] \tag{3}$$

In Eq. (3), $\alpha_{ref}$ represents the resistance temperature coefficient. Eqs. (2) and (3) can be used to determine resistive losses in the wire windings after electrical resistances are obtained. Ohmic heating is defined as the heat dissipation of a conductor when a current passes through it. It is also referred to as resistive heating or joule heating.

$$\dot{E}_g = i(V_A - V_B) = i^2R \tag{4}$$

In the equation Joule-Lenz law or Joule's 1st law, $V_A$ - $V_B$ represents the voltage drop across the conductor, $R$ represents the resistance of the conductor and $i$ represents the current.

$$\dot{q} = \frac{i^2R}{V} \tag{5}$$

If the heat release is uniform within a certain volume ($V$), the volume heat production rate ($\dot{q}$) is expressed by Eq. (5) above [40,41].

Heat transfer is defined as the thermal energy transfer resulting from the spatial temperature difference. Heat transfer takes place in three forms as transmission, transport and radiation. In cases where radiation and transport are effective, the equation expressing heat transfer is derived from the sum of both processes [41].

$$q = q_{conv} + q_{rad} \tag{6}$$

Experimental relationships need to be known in solving heat transfer problems occurring in external natural convection flows. In many engineering calculations, it is sufficient to express relations in the following way [41,42].

$$\overline{Nu}_L = \frac{\overline{h}L}{k} = CRa_L^n \tag{7}$$

The Rayleigh number used in the Eq. (7) above is defined as follows.

$$Ra_L = Gr_L Pr = \frac{g\beta(T_s - T_\infty)L^3}{\upsilon\alpha} \tag{8}$$

All material properties used in the Eq. (7) and Eq. (8) are determined using film temperature ($T_f$).

$$T_f = \frac{T_s + T_\infty}{2} \tag{9}$$

For vertical plates, similar expressions were used for the Nusselt number [42–44]. In case of laminar flow, Rayleigh number is $10^4 \leqslant Ra_L \leqslant 10^9$, $C = 0.59$, and $n = 1/4$. An expression (Eq. (10)) that can be used for all values of the Rayleigh number is also available in the literature [45].

$$\overline{Nu}_L = 0.68 + \frac{0.670Ra_L^{1/4}}{[1+(0.492/Pr)^{9/16}]^{4/9}} \quad Ra_L \leqslant 10^9 \tag{10}$$

Horizontal plates, unlike vertical plates, are evaluated separately as upper and lower plates due to the effect of the lift force created by density difference. In the engineering problems Nusselt number is obtained in the form of Eq. (11) for the upper surface hot plate or the lower surface cold plate when the Rayleigh number is in the range of $10^4 \leqslant Ra_L \leqslant 10^7$ [46].

$$\overline{Nu}_L = 0.54Ra_L^{1/4} \tag{11}$$

Similarly, Nusselt number for the lower surface of the hot plate or the upper surface of the cold plate is obtained in the form of Eq. (12) [47]. Similar relationships are also available in the literature if needed [48].

$$\overline{Nu}_L = 0.52Ra_L^{1/5} \quad 10^4 \leqslant Ra_L \leqslant 10^9, \quad Pr \geqslant 0.7 \tag{12}$$

*Magnetic circuit*

The basic equation for obtaining a magnetic field (Eq. (13)) is defined as the Ampere law [49,50].

$$\oint \mathrm{H}\cdot \mathrm{dl} = \mathrm{I}_{\mathrm{net}} \tag{13}$$

In the above equation, $H$ is the magnetic field density, $dl$ is the differential element defined along the line through which the integral is taken, and $I_{net}$ is the net current that provides the magnetic field. In order to increase the effect of current on the magnetic field density, it is necessary to increase the number of conductors carrying the current, or to place it in such a way as to affect the ferromagnetic material (magnetic core) several times. If the core used to obtain the magnetic field is a ferromagnetic material, the magnetic flux remains within the core and the average length of the core of the $l_c$ core can be written instead of the integral expression in Eq. (14).

$$Hl_c = NI \tag{14}$$

In the above equation, $N$ is the number of turns of wire winding. The magnetic field density $H$ represents the intensity of the magnetic field. The intensity of the magnetic field flux obtained at the core is influenced by the properties of the core material. The density of the magnetic field represents the effort spent to obtain the magnetic flux. The magnetic permeability of the material is a determining factor in the success of this effort. The magnetic flux density ($B$) is defined in Eq. (15) as follows, depending on the material.

$$B = \mu H \tag{15}$$

In the above equation, $\mu$ represents the magnetic permeability of the material. $B$ - $H$ curves are used to determine the magnetic permeability. $B$ - $H$ curves of the MRFs used in this study are given in Fig. 2.

For magnetic cores used in magnetic applications, magnetic materials with relatively high magnetic permeability are preferred. $B$ - $H$ curves for the magnetic core materials used in this study are also given in Fig. 2. The magnetic flux density to be formed in the core is expressed by the following equation.

$$B = \mu H = \frac{\mu Ni}{l_c} \tag{16}$$

The total flux in a given area is defined by the Eq. (17).

$$\Phi = \int_A B\cdot dA \tag{17}$$

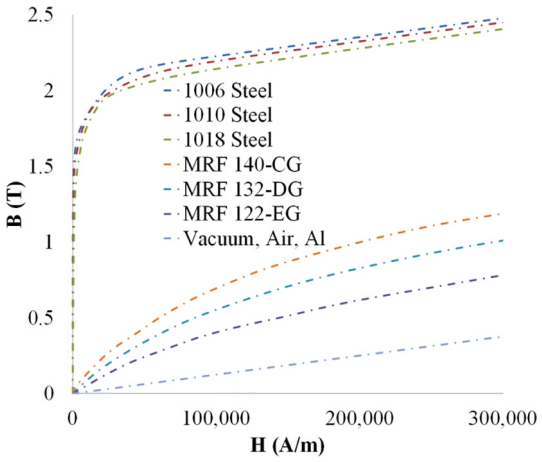


**Fig. 2.** **B** – **H** Curves.

If the flux density vector is perpendicular to the area and the flux density does not change over the entire area, then the above equation can be written in the simplest form.

$$\Phi = BA \tag{18}$$

In cases where the magnetic core geometry allows for regular flux density, the total flux value at the core can be obtained with Eq. (18) above. The cross-sectional area of the magnetic core is expressed by $A$.

$$\Phi = BA = \frac{\mu NiA}{l_c} \tag{19}$$

Generally, since the area ($A$) varies along the flux path, it is more accurate to perform calculations using the Finite element analysis (FEA) method. The relationship between the magnetomotive force $\mathcal{F}$, the number of turns $N$, and the current $i$ is given by $\mathcal{F} = \mathrm{Ni}$. In magnetic circuits, the relationship between magnetomotive force $\mathcal{F}$, flux $\Phi$, and magnetic resistance $\mathcal{R}$ is expressed as $\mathcal{F} = \Phi\mathcal{R}$. The following equation can be used for the general solution of the magnetic circuit.

$$\mathcal{F}_{tot} = \sum_{i=1}^{n} \frac{B_i}{\mu_i} l_{c_i} = Ni \tag{20}$$

In the above equation, $\mathcal{F}_{\mathrm{tot}}$ is the total magnetomotive force, $N$ is the winding number of the coil, $i$ is the current passing through the coil, $B_i$ is the flux density over the resistances in the magnetic circuit, $\mu_i$ is the magnetic permeability, and $l_{c_i}$ is the average length of each resistor.

The flux obtained by using the magnetic circuit will always give an approximate value [51]. For many materials, the magnetic permeability is expressed by a nonlinear curve due to the magnetic field density. In other words, increasing the current constantly does not mean that the flux will increase. The current given to the magnetic field generating systems are selected so that the curve of the magnetic permeability curve does not pass knee points. When the knee points are passed, a lower performance is obtained from the system and the excessive current causes more heat to damage the system. High current causes the insulation material in conductor wires to become worn out due to excessive heat generation and the wire winding becomes inoperable [51].

*Friction torque*

The greatest advantage of MRF devices is that they require very low power for their control. Haptic interfaces are commonly used in force-feedback remote control and virtual training systems.

Especially small, lightweight, low friction and high force capacity actuators are preferred in these interfaces. Despite the fact that MRF devices have the potential to meet these expectations, much of the research has given priority to the investigation of large-scale MRF brakes and dampers, and the generated response torque. The Bingham model is sufficient to calculate the response torque values for MRF brakes operated at low rpms in haptic applications. The frictional torque is usually determined experimentally under zero-field conditions.

The scales provided by the manufacturer are usually used to calculate the friction values due to the use of the O-ring. If the resulting friction forces are very low compared to the other forces in the system, these forces are usually either ignored or determined experimentally. The frictional force acting in the opposite direction to the movement is influenced by the O-ring's nest dimensions, the dimensions of the moving piece, the tightness gap and the rigidity of the sealing element. The friction force is also influenced by the pressure changes that occur due to the operation of the system [52]. The reaction torque due to O-Ring usage can be calculated approximately as follows.

$$T_{O-Ring} = (f_c L_c + f_h A_r) R_s \tag{21}$$

In the Eq. (21), $L_c$ represents the surface length of the seal, $f_c$ represents the friction force per unit length due to the hardness of the orifice and the amount of compression, $f_h$ represents the frictional force due to the fluid pressure, and $A_r$ represents the surface area applied by the fluid. The second component in the equation can be ignored for the reason that the angular velocity of the rotor and the pressure due to the MRF are very low in MRF devices. Since the MRF in the device does not cause high pressures during operation or inside the device, the use of the O-rings with low compression ratios is sufficient [31].

*Passive resistive torque*

MRF devices work in four different modes namely shear mode, flow mode, squeeze mode and pinch mode [53]. The reaction torque generated in the shear mode is due to the yield stresses on the plate surfaces. Brake, clutch and dampers operating in this mode are usually made up of at least two surfaces that move relative to each other. They usually have cylindrical or disc geometry. MRF behaves like a Newtonian fluid when there is no magnetic field and begins to behave like a Bingham plastic where the yield strength can be electronically controlled by magnetic field effect. The resulting response torque depends on dynamic yield strength and fluid viscosity [54]. At low shear rates, MRF can be modeled using the simple and effective Bingham plastic model. The equation for this model is given below.

$$\tau = \begin{cases} \tau_{yield}(H) + \eta \frac{r\omega}{h} & \tau > \tau_y \\ 0 & \tau \leqslant \tau_y \end{cases} \tag{22}$$

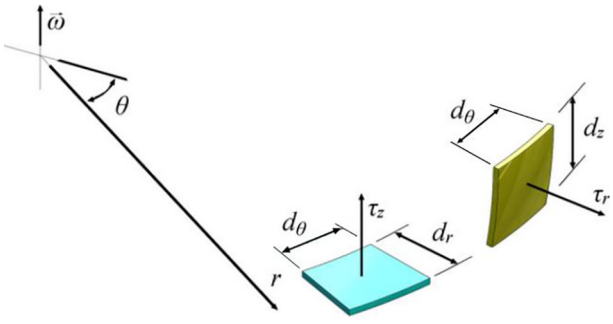


**Fig. 3.** Infinitesimal field elements in devices operating in shear mode.

In the Eq. (22), $\tau$ represents the shear strength, $\tau_{yield}(H)$ represents the dynamic yield strength, $\eta$ is the fluid viscosity, $r$ is the radial distance, $\omega$ is the angular velocity, and $h$ is the distance between the magnetic poles.

The response torque, which is induced in MRF devices operating in shear mode, originates from yield stresses at the surfaces of the disc (Fig. 3). The infinitesimal reaction torque due to these yield stresses, which are the resultant stresses of the MRF flowing between the surfaces, are expressed as follows.

$$dT = 2r\tau_z r d\theta dr + r\tau_r r d\theta dz \tag{23}$$

In disc type MRF devices, due to the disc geometry, the reaction torque in the thin edge of the device is often ignored by the fact that the edge is thin. For this reason, the reaction torque is given by integrating the shear stress along the axial surface.

$$T = 2\pi \int_{r_i}^{r_o} 2\tau_z r^2 dr \tag{24}$$

In Eq. (24), $T$ is the response torque, $r_i$, and $r_o$ respectively represent the inner and outer radius values of the axial surface. If the equation for the Bingham plastic model is written in the above equation, the response torque takes the following form.

$$T = \frac{4\pi}{3}\tau_y(H)(r_o^3 - r_i^3) + \frac{\pi\eta\omega}{h}(r_o^4 - r_i^4) \tag{25}$$

In Eq. (25), the first expression represents the response under the influence of the magnetic field, in other words the MR effect. The second expression represents the reaction torque due to the viscosity of the fluid. If the MRF device is operating at low angular velocities, the second statement will be at a level that can be ignored.

In drum type MRF devices, the first expression in the Eq. (23) is ignored because of its cylindrical geometry. Therefore, by integrating the shear resistance along the radial surface, the response torque is obtained as follows.

$$T = 2\pi \int_0^h \tau_z r^2 dz \tag{26}$$

The Bingham plastic model replaces the equation in the form of response torque in the following manner. In the Eq. (27) and Eq. (28) below, $r$ is the average radius.

$$T = r(2\pi r)h\tau_y(H) + r\frac{2\pi r^2\eta\omega}{\mathrm{t}}h \tag{27}$$

Similarly, the effect of the viscous component in the equation can be ignored if the device is considered to operate at low angular velocities.

For devices operating in flow mode, the pressure drop consists of the viscous component $\Delta P_{rheo}$ and the magnetic field dependent $\Delta P_{mrf}$ components [26,54–58]. The total reaction torque is obtained by the addition of friction, viscous and magnetic effects. The approximate expression used to obtain the total reaction torque is given below.

$$T = T_{friction} + rA\Delta P_{rheo} + rA\Delta P_{mrf} \tag{28}$$

The viscous component is so small that it can be ignored in calculations. The equations for the pure viscous effect ($\Delta P_{rheo}$) and the magnetic field dependent component ($\Delta P_{mrf}$) are given below.

$$\Delta P_{rheo} = \frac{12\eta QL}{th^3} \tag{29}$$

$$\Delta P_{mrf} = \frac{3\tau_{yield}(H)L}{h} \tag{30}$$

$$A = th \tag{31}$$

In the above equations, $\eta$ represents the viscosity of the fluid, $Q$ is the flow through the pressure drop, $L$ represents the length of the flow channel, $t$ represents the width of the plates, and $h$ represents the gap between the plates. It is understood from the related equations that the flow channel area is the product of the values of $t$ and $h$, which is defined as $A = th$. The $\tau_{yield}(H)$, which represents the yield strength, depends on the magnetic field strength. Where the ratio of the radial distance value of the flow channel measurements of a device operating in flow mode is small, the expression of a linear device for the device's response torque can be used. FEA simulations are used in the optimization process. This method is one of the preferred approaches in the design of such devices. Conversely using FEA requires a lot of computational time and power during optimization problems.

## Modified PSO algorithm

Millonas stated [59] swarm intelligence must be able to change behavior mode when it is worth the computational price. A reinforced (common) PSO equation with inertia weight by Shi ve Eberhart [60] were given as:

$$v_{k+1} = wv_k + c_1 r_1(xbest_k - x_k) + c_2 r_2(xgbest_k - x_k) \tag{32}$$

$$x_{k+1} = x_k + v_{k+1} \tag{33}$$

where $x_k$, $v_k$ are the particle's $k^{th}$ position and velocity vector; $r_1$ and $r_2$ are random numbers ranging in (1,0); $xbest_k$ and $xgbest_k$ are the $k^{th}$ best positions by the particle and the whole swarm; $c_1$ and $c_2$ are two parameters representing the particle's confidence as an individual and as a member of the whole swarm; $w$ is inertia weight which is used to maintain balance between shrinking of search space and global search tendency. The parameters $c_1$ and $c_2$ control the balance between local search and global search and are generally set to 2 [4].

When particles are created or during the optimization process, if the best position of a particle is equal to the best position of the swarm and also if velocity of the particle is zero, that particle will come to a halt. Randomness will provide the particle, even those that don't move, with the capability to search even more [61–63]. After the initialization of the swarm or during optimization progress such stuck particles may affect the whole swarm undesirably. With the intention of getting over such situations a random disturbance is added to calculation of the particle's next position.

$$x_{k+1} = x_k + v_{k+1} + d \tag{34}$$

where $d$ is a small random number which pulls or pushes the particle a little bit to provide a continuous search even after reaching the best possible position. The PSO algorithm [64] with a random disturbance is given in Fig. 4.

With the purpose of preventing particles from leaving the search space Eberhart et al. [65] introduced a maximum velocity parameter, $V_{max}$. In addition to limitation of velocity, another approach is used by Nguyen et al. [66]. This approach, known as gradient-based repair method [67], is summarized below.

Step 1. Calculate the degree of violation of constraints

$$\Delta \boldsymbol{V} = \left[\frac{Min\langle \boldsymbol{0}, \boldsymbol{u} - \boldsymbol{g}(\boldsymbol{x})\rangle + Max\langle \boldsymbol{0}, l - \boldsymbol{g}(\boldsymbol{x})\rangle}{\boldsymbol{h}(\boldsymbol{x}) - \boldsymbol{c}}\right] \tag{35}$$

where $g_m(\boldsymbol{x})$ and $h_n(\boldsymbol{x})$ respectively refer to inequality and equality constraints.

Step 2. Calculate $\nabla_{\boldsymbol{x}}\boldsymbol{V}^+$ and $\Delta\boldsymbol{x}$. For the calculation of value $\nabla_{\boldsymbol{x}}\boldsymbol{V}^+$, it is necessary to take the inverse of Moore-Penrose [68] of the matrix $\nabla_{\boldsymbol{x}}\boldsymbol{V}$.

```
For every particle
  initialize x, v and xbest
End
Do
  For every particle
    evaluate objective function
    If (xbest_k>xbest_k-1) update xbest
  End
  update gbest with the best xbest
  For every particle
    calculate v
    update x=x+v+d
  End
While (not termination condition)
```

**Fig. 4.** Pseudocode for the PSO algorithm with a random disturbance.

$$\Delta \boldsymbol{V} = \nabla_{\boldsymbol{x}}\boldsymbol{V} \times \Delta \boldsymbol{x} \tag{36}$$

$$\Delta \boldsymbol{x} = \nabla_{\boldsymbol{x}}\boldsymbol{V}^{-1} \times \Delta \boldsymbol{V} \tag{37}$$

Step 3. Update the solution vector using the following equation.

$$\boldsymbol{x}^{t+1} = \boldsymbol{x}^t + \nabla_{\boldsymbol{x}}\boldsymbol{V}^+ \times \Delta \boldsymbol{V} \tag{38}$$

Step 4. If the solution vector is not in the desired region after repair, the process can be repeated [67].

Improving the exploration ability of PSO has been a popular research topic in recent years [69]. In this study, similar to Kennedy and Eberhart's [4] conversion of the social simulation algorithm into an optimization paradigm by replacing "roost" by "food", a better optimization algorithm is achieved by replacing "food" by "prey".

In the wild, hunters must use their resources in the best possible way. In other words, proper use of limited resources is a matter of life and death. The general approach in common PSO is based on the uncovering of food resources and summoning the swarm to the current ideal positions. But this approach can have very dangerous consequences for a swarm with limited resources. PSO performs best at or near the center of the initialization region [70]. In this study we tried to mimic an approach which resembles a hunting swarm. The hunting PSO is summarized below.

- Determine the location of the most ideal food source with a subswarm, like targeting of the most promising herd
- Initialize another subswarm that can carry out the work that requires more resources, like leaving the prey vulnerable or alone
- Initialize the last subswarm to end the hunt.

The hunting capability is simply simulated by using the best location of previous subswarm for initialization of the next one.

## Multi-objective multi-physics engineering design optimization problem

Distinct from the common PSO, the parameters that do not have much effect at the beginning of the optimization process are performed by the second subswarm of the hunting PSO. The magnetic core material, wire type, and the MR fluid type are features that have very little effect at the beginning of the optimization process. In this study, only the effect of wire type selection was performed by the second subswarm of the hunting PSO.

**Begin**
**Set** wire type to AWG 26
**Begin** PSO code for the 1st subswarm with **15 particles** up to **4 iterations**
Get the highest permissible current
Carry out torque, mass and power calculations for all three steel and MR fluid configurations
**End**
**Set** wire types to AWG 24, AWG 26, & AWG 28
**Set** initialization positions around the previous subswarm's global best
**Begin** PSO code for the 2nd subswarm with **5 particles** up to **4 iterations**
Get the highest permissible current
Carry out torque, mass and power calculations for every steel, wire and MR fluid configurations
**End**
**Get** the best wire type from previous subswarm
**Set** initialization positions around the previous subswarm's global best
**Begin** PSO code for the last subswarm with **5 particles** up to **12 iterations**
Get the highest permissible current
Carry out torque, mass and power calculations for all three steel and MR fluid configurations
**End**
**End**

**Fig. 5.** Pseudocode of the hunting PSO.

**Begin**
**Set** wire types to AWG 24, AWG 26 & AWG 28
**Initialize** the swarm with **15 particles** up to **12 iterations**
Get the highest permissible current
Carry out torque, mass and power calculations for all three steel, wire and MR fluid configurations
**End**

**Fig. 6.** Pseudocode of the common PSO.

**Begin**
**Read** device dimensions and inputs
Calculate wire length and resistance using wire diameter and number of turns
Calculate joule heating with Eq. (4) and volumetric heat production with Eq. (5)
Calculate Rayleigh, Nusselt numbers and the coefficients required for heat transfer analysis with the help of relevant equations
Calculate only the convective heat transfer coefficients for the initial calculation
**Do**
Perform heat transfer analysis of the system
Get the outside temperature of the device
Update the amount of heat transfer by convection and radiation taking into account equations related to bottom, top, and vertical plates
Obtain a general heat transfer equation
Update convective heat transfer coefficients
**While** (error at surface temperature > $1x10^{-3}$)
**End**

**Fig. 7.** Pseudocode of the heat transfer analysis.

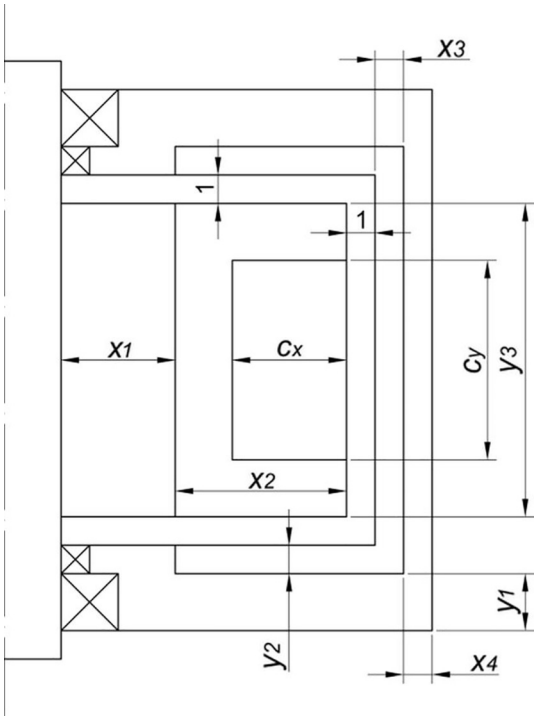


**Fig. 8.** Hybrid-type (device 0) MRF brake's dimensional parameters.

*Cost/fitness function*

The following multi-objective total cost/fitness function has been used in order to obtain the design with the highest torque, lowest electrical power consumption, and lowest mass. The cost function used for the hunting PSO is given below.

$$Cost\ Function = \frac{Mass\ [g] \cdot Power\ [W]}{Torque\ [mN.m]} \tag{39}$$

*Algorithms*

Both algorithm for the hunting PSO and algorithm for the common PSO are given below (Figs. 5, 6 and 7). While general PSO performs all calculations in one go, hunting PSO solves the calculations that need to be done with the help of subwarms. The second and third subswarms of the hunting PSO are re-initialized around the previous subswarm's global best.

Three subswarms were created for the Hunting PSO used in this study. This number can be changed for different problem types. The first subswarm was created using three times more particles than the other subswarms. In this way, a more efficient search could be performed in a larger search space. The second subswarm calculates the cost function with all the optimization parameters using only 5 particles. The last subswarm iterates three times more than the other subswarms. Thus, the last subswarm can detect optima in a much smaller search space. The algorithm, unlike common PSO, starts an optimization process in a smaller search space with each subswarm.

The highest permissible current is obtained by carrying out a heat transfer analysis. The pseudocode for the heat transfer analysis is given below.

*Rotary MRF brakes' base designs*

Hunting PSO and common PSO were compared using four different rotary MRF brake designs. Each brake was optimized using

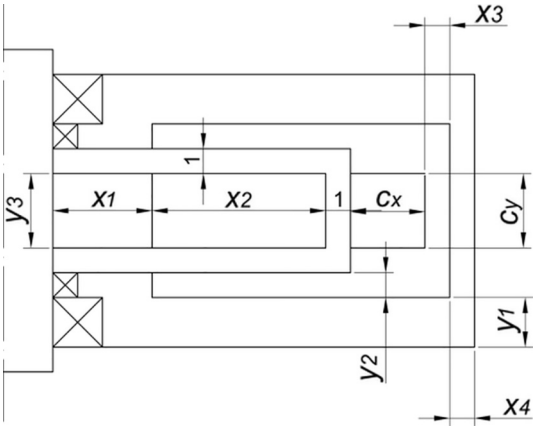


**Fig. 9.** Disc type (device 1) MRF brake's dimensional parameters.

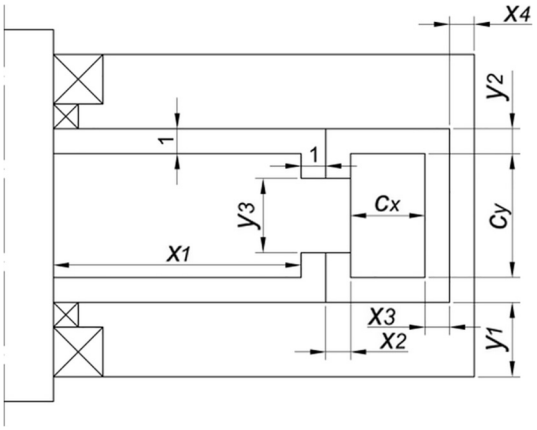


**Fig. 10.** Rotary flow mode (device 2) MRF brake's dimensional parameters.

three magnetic core materials, three MR fluids, and three wire types. The dimensional parameters of the MRF brakes are shown in the following figures. In all the figures, the bearings are shown with large crossed squares and O-rings are shown as small crossed squares which are placed upper and lower parts of the shaft. All designs are confined to a maximum outer radius of 25 mm and have MRF gaps with a thickness of 1 mm.

Fig. 8 shows the hybrid-type (device 0) MRF brake configuration where the coil is placed inside the shaft. Fig. 9 shows the disc type (device 1) MRF brake's dimensional parameters.

Fig. 10 shows the rotary flow mode (device 2) MRF brake in which MRF is forced the flow between the poles of the electromagnet. Details of the working mode and design details of the rotary flow mode MRF brake are available in the literature [26].

T-Shape (device 3) MRF brake's dimensional parameters are given in Fig. 11. The equality and inequality constraints of the MRF brakes used in calculations for each type of device are given in Table 1.

## Results

### *Results of hunting PSO*

PSO initiates with random placement of particles. This may cause the particles to be too close to or too far from the global or

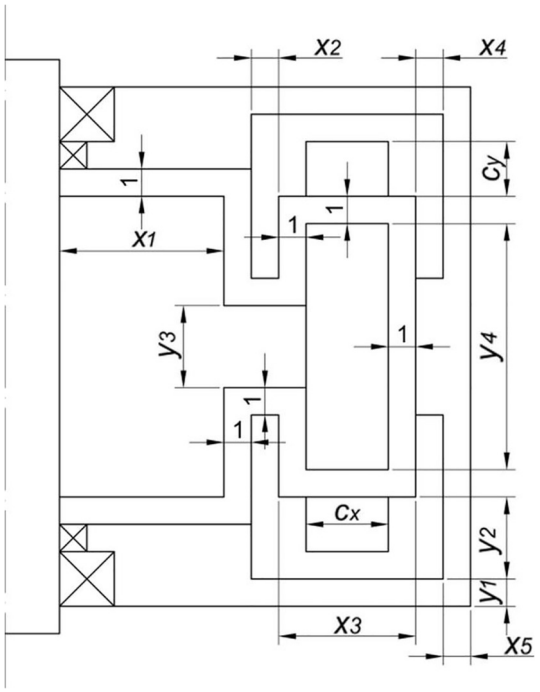


**Fig. 11.** T-Shape (device 3) MRF brake's dimensional parameters.

**Table 1**
Equality and inequality constraints of the MRF brakes.

| parameter [mm] | Device 0 | Device 1 | Device 2 | Device 3 |
|---|---|---|---|---|
| $x_1$ | 1–18 | 1–18 | 1–18 | 1–16 |
| $x_2$ | 2–19 | 1–18 | 1–18 | 1–4 |
| $x_3$ | 1–8 | 1–8 | 1–8 | 3–8 |
| $x_4$ | 1–8 | 1–8 | 1–8 | 1–4 |
| $x_5$ | – | – | – | 1–4 |
| $y_1$ | 2–8 | 2–8 | 3–8 | 1–4 |
| $y_2$ | 1–8 | 1–8 | 1–8 | 2–8 |
| $y_3$ | 4–24 | 1–16 | 1–8 | 2–4 |
| $y_4$ | – | – | – | $(y_3+2)-24$ |
| $c_x$ | $(x_2-1)$ | 1–18 | 1–18 | $1-x_3$ |
| $c_y$ | $(y_3-2)$ | $(y_3+2)$ | 3–24 | $3-(y_2-1)$ |

local optima. The results obtained from the first subswarm are given in Fig. 12. Torque, mass, and power changes due to decreasing cost function values are seen for all four devices. The results show clearly that the positions on the graph are beginning to change regularly and that the optimization is in the beginning phase.

The results obtained from the 2nd subswarm are given in Fig. 13. Torque, mass, and power changes appear linear for each device in comparison with decreasing cost values. It seems that the optimization process continues in a smaller search space as desired.

The results obtained from the last subswarm are given in Fig. 14. In Fig. 14, the cost value for each device design is reduced and the response torque is increased. Mass and power values have changed in a narrow range. Also for all devices, the parameters corresponding to the lowest cost function value that are obtained from each subswarm are given in Table 2.

Table 3 gives the characteristics of the devices which are achieved by hunting PSO. Since the shaft diameters of all four designs are the same, the zero-field torques will be approximately 30 mN.m based on the Eq. (21). Material types used for numerical calculations are given in the figures of heat transfer analyses.

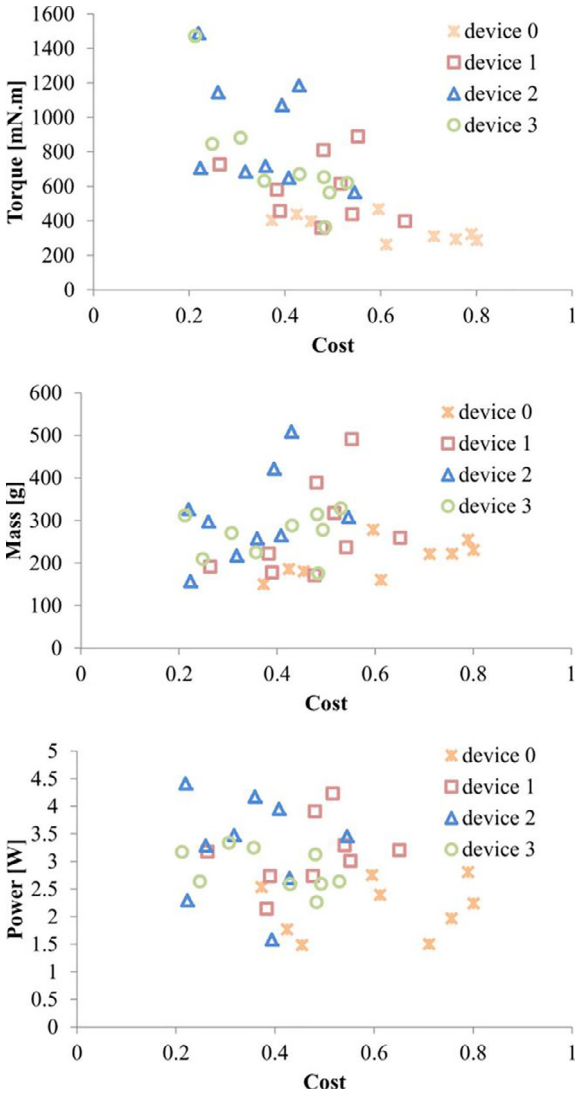


**Fig. 12.** Results from 1st subswarm based on cost function value.

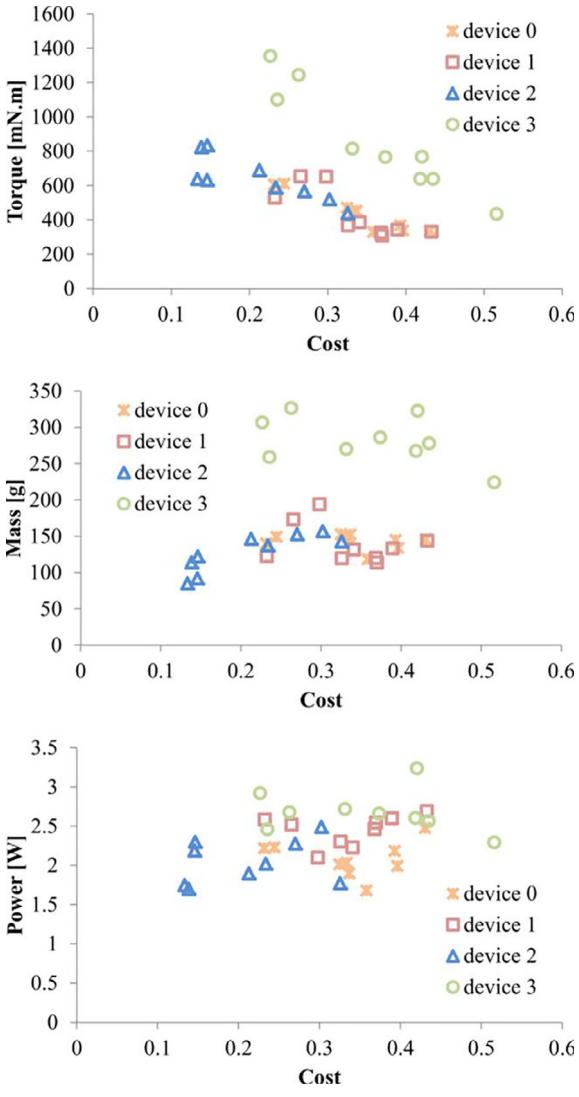


**Fig. 13.** Results from 2nd subswarm based on cost function value.

Figs. 15 and 16 show the magnetic field and heat transfer analysis of the hybrid-type (device 0) MRF device at a current of 1.3 A. Despite the fact that the hybrid-type favors a cylindrical geometry, it has disc geometry because of the mass factor in the cost function.

Figs. 17 and 18 show the magnetic field and heat transfer analyzes of the disc type (device 1) MRF device at a current of 1.0 A. Due to the coil winding and the maximum radius limitation, the geometry is thicker than conventional disc geometry.

Magnetic field analysis and heat transfer analysis of the rotary flow-type MRF brake at a current of 1.8 A are given respectively in Fig. 19 in Fig. 20. The brake resembles the hybrid type and disc type devices. The flow channel of the flow type device is also deepened after optimization. Geometric constraints have forced these three devices to take a thick disc shape. The magnetic field analysis and the heat transfer analysis of the T-shape MRF brake at a current of 1.0 A are given respectively in Fig. 20 and Fig. 21. The brake has cylindrical geometry unlike the other three designs. Likewise this geometry, which is usually seen in drum-type devices, is due to the outer radius limitation.

The regions used in the torque calculations are marked with dashed yellow lines in Fig. 16, Fig. 18, Fig. 20, and Fig. 22. The MR fluid temperatures for device 0, device 1, device 2, and device 3 were obtained approximately 70 °C, 60 °C, 70 °C, and 75 °C. It is seen that the temperature distribution changes depending on the external surface area, position of coil winding, and power input.

*Results of common PSO*

The cost function dependent torque, mass, and power values obtained from the common PSO are given in Fig. 23.

In Table 4, the parameters of the designs obtained at the lowest cost are given.

Table 5 gives the characteristics of the devices which are achieved by common PSO. It is seen that the hunting PSO, which has the lowest cost function value of 0.091, is more successful when Tables 3 and 5 are compared.

1st subswarm's timing is 28.2 h, 2nd subswarm's timing is 22.5 h, and 3rd subswarm's timing is 22.4 h. Total running time for the hunting PSO and the common PSO is respectively 73.1 and 195.8 h. Device 3 has two additional dimensional parameters, which have increased the simulation time by 54% compared to other devices. The hunting PSO required about 1/3 computational time compared to the common PSO. Furthermore hunting PSO

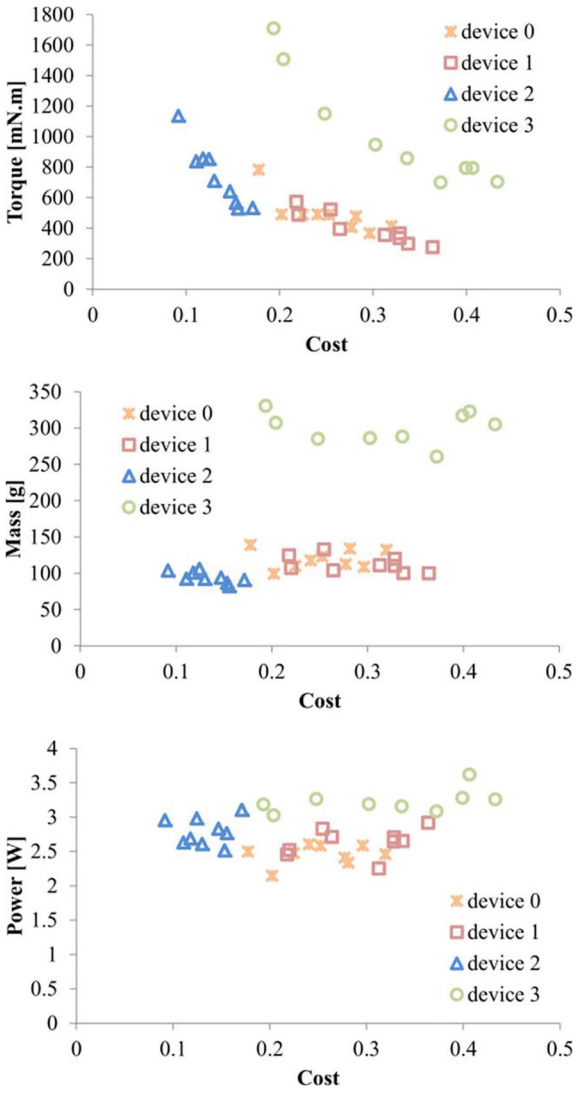


**Fig. 14.** Results from 3rd subswarm based on cost function value.

**Table 2**
Dimensional parameters of the MRF brakes based on hunting PSO with random disturbance.

| parameter [mm] | Device 0 1st, 2nd, and 3rd | Device 1 1st, 2nd, and 3rd | Device 2 1st, 2nd, and 3rd | Device 3 1st, 2nd, and 3rd |
|---|---|---|---|---|
| $x_1$ | 13.1, 12.6, 12.7 | 10.8, 9.5, 8.9 | 11.9, 10.5, 10.1 | 13.2, 12.8, 12.6 |
| $x_2$ | 5.3, 5.9, 6.5 | 9.1, 7.0, 6.8 | 7.6, 6.9, 6.7 | 2.1, 2.4, 2.8 |
| $x_3$ | 2.2, 1.5, 1.7 | 1.7, 1.2, 1.5 | 1.0, 1.4, 1.6 | 3.9, 3.7, 3.5 |
| $x_4$ | 1.3, 1.8, 1.1 | 1.0, 1.0, 1.0 | 1.0, 1.2, 1.1 | 2.2, 2.2, 2.1 |
| $x_5$ | – | – | – | 1.0, 1.0, 1.2 |
| $y_1$ | 3.8, 2.4, 2.2 | 2.9, 2.0, 2.0 | 3.8, 3.0, 3.0 | 2.5, 2.5, 2.7 |
| $y_2$ | 2.1, 1.0, 1.2 | 1.3, 1.5, 1.7 | 3.3, 2.0, 1.8 | 5.9, 5.7, 7.3 |
| $y_3$ | 7.9, 7.3, 7.2 | 4.7, 3.7, 3.8 | 1.4, 1.1, 1.0 | 2.7, 2.7, 3.5 |
| $y_4$ | – | – | – | 21.2, 21.2, 22.1 |
| $c_x$ | 3.1, 2.7, 3.8 | 3.9, 3.7, 3.7 | 2.2, 2.1, 2.5 | 3.6, 3.5, 3.5 |
| $c_y$ | 5.8, 5.3, 4.2 | 6.7, 5.7, 5.8 | 3.0, 2.3, 3.3 | 3.7, 3.7, 4.6 |

could be accelerated even more by controlling steel and fluid type selections. In addition to the given results, all steel types and AWG 26 and AWG 28 wire types were encountered at different iterations of the optimization process. Although MRF 140 CG is

**Table 3**
Optimization results obtained from hunting PSO.

| Results | Device 0 | Device 1 | Device 2 | Device 3 |
|---|---|---|---|---|
| Torque [mN.m] | 783.7 | 574.4 | 1136.8 | 1711.3 |
| Current [A] | 1.3 | 1.0 | 1.8 | 1.0 |
| Power [W] | 2.5 | 2.5 | 3.0 | 3.2 |
| Mass [g] | 139.1 | 125.0 | 104.0 | 330.7 |
| AWG | 26 | 26 | 26 | 26 |
| MRF | 140 CG | 140 CG | 140 CG | 140 CG |
| Steel | 1006 | 1006 | 1006 | 1006 |
| Number of turns | 90 | 126 | 48 | 88 |
| Cost function | 0.178 | 0.218 | 0.091 | 0.193 |

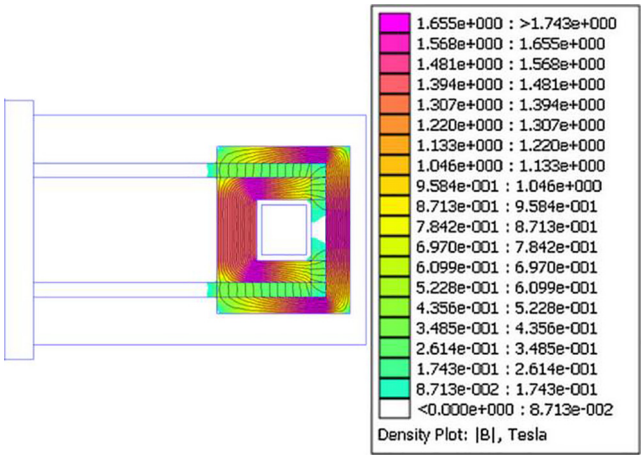


**Fig. 15.** Magnetic field strength of hybrid-type (device 0) MRF brake.

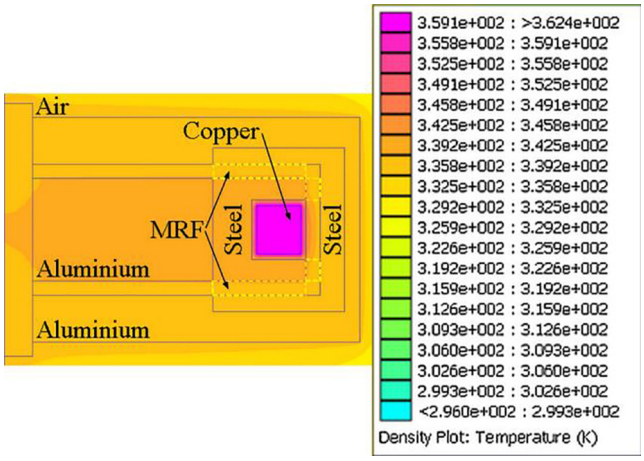


**Fig. 16.** Temperature distribution of hybrid-type (device 0) MRF brake.

common in all results, it is not preferred much for the reason of zero-field high viscous effect. The temperatures obtained are safe for both MRF and wire use. Higher torques can also be obtained by applying higher currents with a wire type that is resistant to higher temperatures. Although the T-shape (device 3) MRF brake produces very high torques, this device is heavier than all other devices. According to the cost function, it seems that the most ideal design for haptic systems is the rotary flow type (device 2) MRF brake with a height of 12.9 mm, a diameter of 50 mm, and a weight of 104 g.

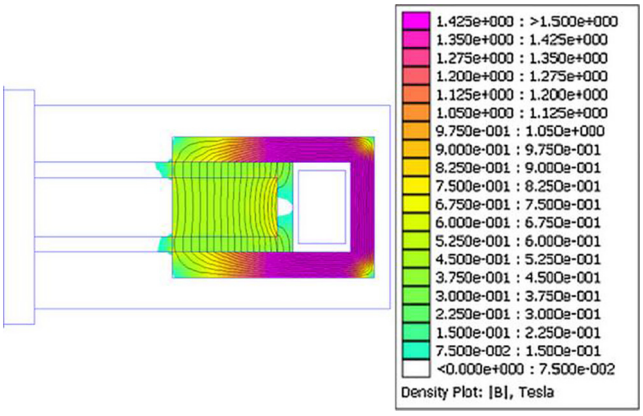


**Fig. 17.** Magnetic field strength of disc type (device 1) MRF brake.

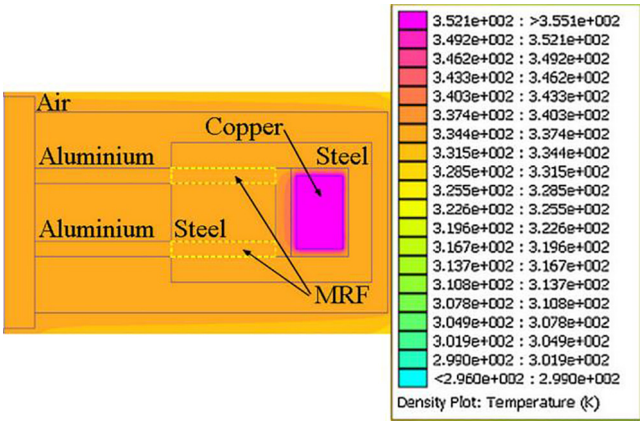


**Fig. 18.** Temperature distribution of disc type (device 1) MRF brake.

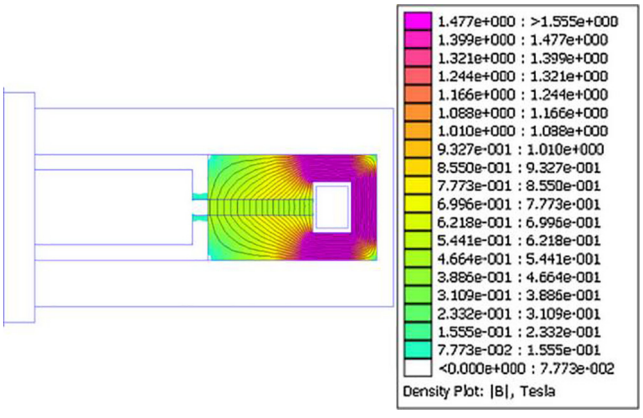


**Fig. 19.** Magnetic field strength of rotary flow type (device 2) MRF brake.

## Conclusions and future work

In this paper four rotary MRF brake designs are optimized by a simple cost function which seeks the highest torque, lowest power consumption, and lightweight designs. The optimization process was carried out by a modified PSO algorithm which was inspired by a hunting party with task distribution. This successfully developed and modified PSO algorithm with multiple subpopulations has solved a multi-physics optimization problem. The modified PSO algorithm begins with a relatively large subpopulation with limited resources. The first large subswarm is expected to uncover a solution space around the best possible solution. Narrowing of this search space is carried by a small subswarm with relatively

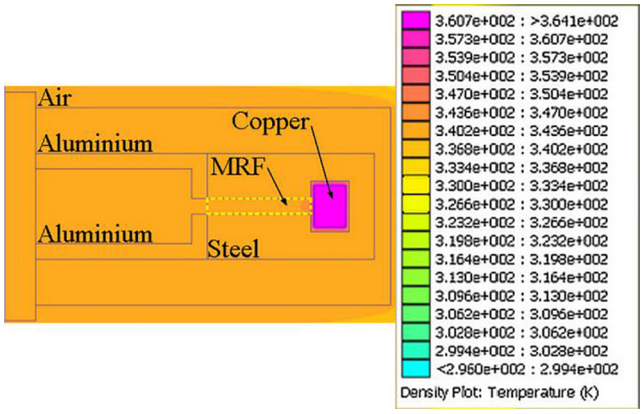


**Fig. 20.** Temperature distribution of rotary flow type (device 2) MRF brake.

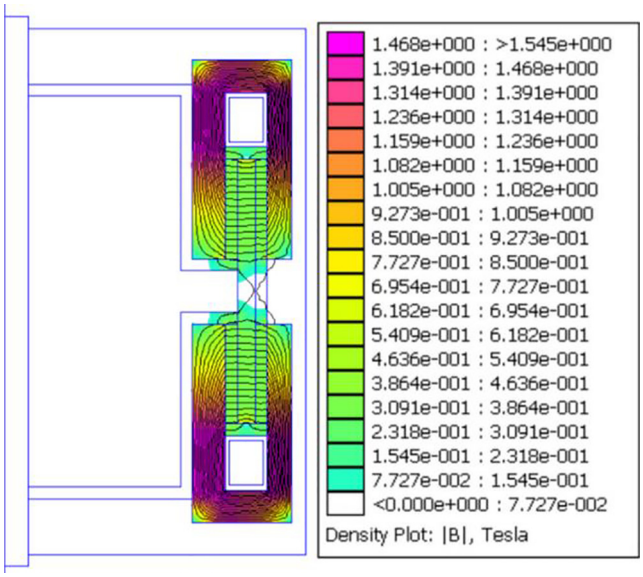


**Fig. 21.** Magnetic field strength of T-shape type (device 3) MRF brake.

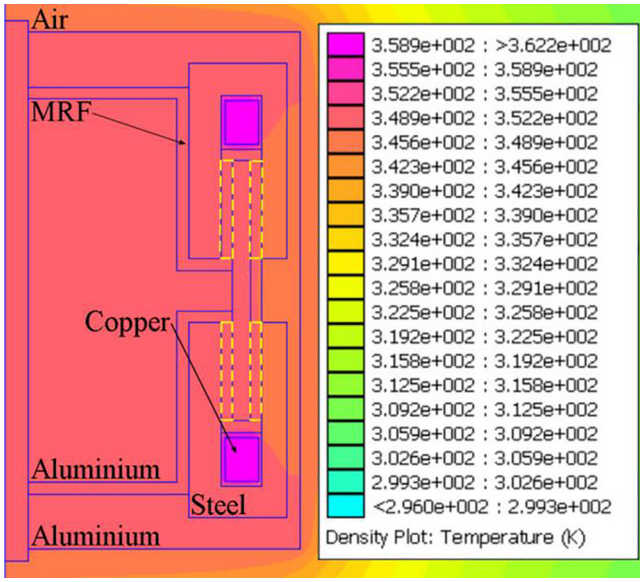


**Fig. 22.** Temperature distribution of T-shape (device 3) MRF brake.

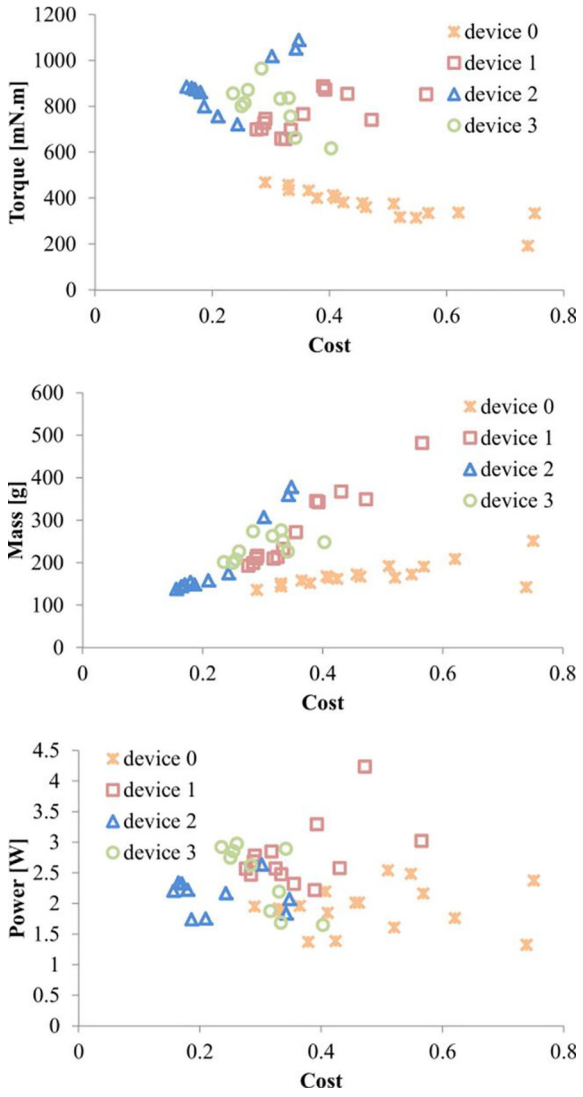


**Fig. 23.** Results obtained from common PSO.

**Table 4**
Dimensional parameters of the MRF brakes based on common PSO with random disturbance.

| parameter [mm] | Device 0 | Device 1 | Device 2 | Device 3 |
|---|---|---|---|---|
| $x_1$ | 11.6 | 4.3 | 9.2 | 12.4 |
| $x_2$ | 5.2 | 12.3 | 7.4 | 1.9 |
| $x_3$ | 1.5 | 2.0 | 1.2 | 3.7 |
| $x_4$ | 3.8 | 1.2 | 1.2 | 1.2 |
| $x_5$ | – | – | – | 1.0 |
| $y_1$ | 3.0 | 4.3 | 3.1 | 1.5 |
| $y_2$ | 1.4 | 2.1 | 2.6 | 4.8 |
| $y_3$ | 7.1 | 5.6 | 1.0 | 2.6 |
| $y_4$ | – | – | – | 16.2 |
| $c_x$ | 3.1 | 2.1 | 3.2 | 3.1 |
| $c_y$ | 5.1 | 7.2 | 4.5 | 3.3 |

large resources that is fully capable of searching the space. The locating of optimal positions is carried out by the last subswarm which has also limited resources but has the knowledge of the small search space where the best solution resides. Obtained results sufficiently reveal the applicability of the modified PSO algorithm in similar multi-physics problems. In future works, the modified PSO algorithm may be applied to solve the multimodal multi-objective engineering optimization problems.

**Table 5**
Optimization results obtained from common PSO.

| Results | Device 0 | Device 1 | Device 2 | Device 3 |
|---|---|---|---|---|
| Torque [mN.m] | 469.0 | 700.6 | 1136.8 | 1711.3 |
| Current [A] | 1.3 | 1.3 | 1.3 | 1.3 |
| Power [W] | 2.0 | 2.6 | 2.2 | 2.9 |
| Mass [g] | 136.1 | 193.2 | 138.1 | 201.7 |
| AWG | 26 | 26 | 26 | 26 |
| MRF | 140 CG | 140 CG | 140 CG | 140 CG |
| Steel | 1010 | 1006 | 1018 | 1010 |
| Number of turns | 84 | 85 | 77 | 56 |
| Cost function | 0.29 | 0.276 | 0.156 | 0.235 |

## Declaration of conflicting interests

The author(s) declared no potential conflicts of interest with respect to the research, authorship, and/or publication of this article.

## Funding

This research received no specific grant from any funding agency in the public, commercial, or not-for-profit sectors.

## Appendix A. Supplementary data

Supplementary data associated with this article can be found, in the online version, at https://doi.org/10.1016/j.rinp.2018.01.007.

## References

[1] Lari A, Khosravi A, Rajabi F. Controller design based on analysis and PSO algorithm. ISA Trans 2014;53:517–23. https://doi.org/10.1016/j.isatra.2013.11.006.
[2] Chiou JS, Tsai SH, Liu MT. A PSO-based adaptive fuzzy PID-controllers. Simul Model Pract Theory 2012;26:49–59. https://doi.org/10.1016/j.simpat.2012.04.001.
[3] Letting LK, Munda JL, Hamam Y. Optimization of a fuzzy logic controller for PV grid inverter control using S-function based PSO. Sol Energy 2012;86:1689–700. https://doi.org/10.1016/j.solener.2012.03.018.
[4] Kennedy J, Eberhart C. Particle swarm optimization. In: Proceeding IEEE Int. Conf. Neural Networks, Perth, Australia; 1995, p. 1942–8.
[5] Reeves WT. Particle systems – a technique for modeling a class of fuzzy objects. ACM SIGGRAPH Comput Graph 1983;17:359–75. https://doi.org/10.1145/964967.801167.
[6] Reynolds CW. Flocks, herds and schools: a distributed behavioral model. ACM SIGGRAPH Comput Graph 1987;21:25–34. https://doi.org/10.1145/37402.37406.
[7] Chang W. A modified particle swarm optimization with multiple subpopulations for multimodal function optimization problems. Appl Soft Comput J 2015;33:170–82. https://doi.org/10.1016/j.asoc.2015.04.002.
[8] Krishnanand KN, Ghose D. Glowworm swarm optimization for simultaneous capture of multiple local optima of multimodal functions. Swarm Intell 2009;3:87–124. https://doi.org/10.1007/s11721-008-0021-5.
[9] Yazdani S, Nezamabadi-Pour H, Kamyab S. A gravitational search algorithm for multimodal optimization. Swarm Evol Comput 2014;14:1–14. https://doi.org/10.1016/j.swevo.2013.08.001.
[10] Chen C-C. Two-layer particle swarm optimization for unconstrained optimization problems. Appl Soft Comput 2011;11:295–304. https://doi.org/10.1016/j.asoc.2009.11.020.
[11] Peng Y, Lu B-L. A hierarchical particle swarm optimizer with latin sampling based memetic algorithm for numerical optimization. Appl Soft Comput 2012. https://doi.org/10.1016/j.asoc.2012.05.020.
[12] Wang H, Yang S, Ip WH, Wang D. A memetic particle swarm optimisation algorithm for dynamic multi-modal optimisation problems. Int J Syst Sci 2012;43:1268–83. https://doi.org/10.1080/00207721.2011.605966.
[13] Otani T, Suzuki R, Arita T. DE/isolated/1: a new mutation operator for multimodal optimization with differential evolution. Int J Mach Learn Cybern 2013;4:99–105. https://doi.org/10.1007/s13042-012-0075-y.
[14] Kaveh A, Laknejadi K. A new multi-swarm multi-objective optimization method for structural design. Adv Eng Softw 2013;58:54–69. https://doi.org/10.1016/j.advengsoft.2013.01.004.
[15] Goh CK, Tan KC, Liu DS, Chiam SC. A competitive and cooperative co-evolutionary approach to multi-objective particle swarm optimization algorithm design. Eur J Oper Res 2010;202:42–54. https://doi.org/10.1016/j.ejor.2009.05.005.

[16] Nekouie N, Yaghoobi M. A new method in multimodal optimization based on firefly algorithm. Artif Intell Rev 2016;46:267–87. https://doi.org/10.1007/s10462-016-9463-0.
[17] Glibovets NN, Gulayeva NM. A review of niching genetic algorithms for multimodal function optimization. Cybern Syst Anal 2013;49:815–20. https://doi.org/10.1007/s10559-013-9570-8.
[18] Rabinow J. The magnetic fluid clutch. Trans Am Inst Electr Eng 1948;67:1308–15. https://doi.org/10.1109/T-AIEE.1948.5059821.
[19] Mid-Atlantic Rubber – Magneto-rheological (MR) STORE n.d.
[20] Baranwal D, Deshmukh T. MR-fluid technology and its application – a review. Int J Emerg Technol Adv Eng 2012;2:563–9.
[21] Shimoga K. Finger force and touch feedback issues in dexterous telemanipulation. in: Proceedings Fourth Annu Conf Intell Robot Syst Sp. Explor., 1992, p. 159–78. doi:10.1109/IRSSE.1992.671841.
[22] Demersseman R, Hafez M, Lemaire-Semail B, Clenet S. Magnetorheological Brake for Haptic Rendering Haptics: Perception, Devices and Scenarios. Haptics Perception, Devices Scenar. Springer: Berlin Heidelberg; 2008, p. 941–5. doi: 10.1007/978-3-540-69057-3_119.
[23] Senkal D, Gurocak H. Serpentine flux path for high torque MRF brakes in haptics applications. Mechatronics 2010;20:377–83. https://doi.org/10.1016/j.mechatronics.2010.02.006.
[24] Kikuchi T, Ikeda K, Otsuki K, Kakehashi T, Furusho J. Compact MR fluid clutch device for human-friendly actuator. J Phys Conf Ser 2009;149:12059. https://doi.org/10.1088/1742-6596/149/1/012059.
[25] Colgate JE, Stanley MC, Schenkel G. Dynamic range of achievable impedances in force reflecting interfaces. In: Kim WS, editor. Proc. SPIE 2057, Telemanipulator Technol. Sp. Telerobotics, 199, vol. 2057, International Society for Optics and Photonics; 1993, p. 199–210. doi: 10.1117/12.164900.
[26] Topcu O, Tascioglu Y, Konukseven EI. A Novel Rotary Magneto-Rheological Damper for Haptic Interfaces. Vol. 4B Dyn. Vib. Control, vol. 4B–2015, ASME; 2015, p. V04BT04A056. doi: 10.1115/IMECE2015-50979.
[27] J. Colgate J. Brown Factors affecting the Z-Width of a haptic display. Proc. IEEE Int Conf. Robot. Autom. 1994 1994 3205 10 10.1109/ROBOT.1994.351077.
[28] Assadsangabi B, Daneshmand F, Vahdati N, Eghtesad M, Bazargan-Lari Y. Optimization and design of disk-type MR brakes. Int J Automot Technol 2011;12:921–32. https://doi.org/10.1007/s12239-011-0105-x.
[29] Li W, Yadmellat P, Kermani MR. Design optimization and comparison of magneto-rheological actuators. Proc – IEEE Int Conf Robot Autom; 2014, p. 5050–5. doi: 10.1109/ICRA.2014.6907599.
[30] Blake J, Gurocak HB. Haptic glove with MR brakes for virtual reality. IEEE/ASME Trans Mechatron 2009;14:606–15. https://doi.org/10.1109/TMECH.2008.2010934.
[31] Nguyen QH, Lang VT, Nguyen ND, Choi SB. Geometric optimal design of a magneto-rheological brake considering different shapes for the brake envelope. Smart Mater Struct 2014;23:15020. https://doi.org/10.1088/0964-1726/23/1/015020.
[32] NFPA A. 70-National Electrical Code. Natl Fire Prot Assoc; 2005 1.
[33] Fuller MA. Heat transfer characteristics of mining cables. Conf Rec IEEE Ind Appl Soc Annu Meet, IEEE; n.d., p. 1503–8. doi: 10.1109/IAS.1989.96841.
[34] Wang DM, Hou YF, Tian ZZ. A novel high-torque magnetorheological brake with a water cooling method for heat dissipation. Smart Mater Struct 2013;22:25019. https://doi.org/10.1088/0964-1726/22/2/025019.
[35] Huang J, Qiao Z, Fan B. Properties of MR Transmission under Thermal Affect. Or.nsfc.gov.cn n.d.
[36] Weiss KD, Duclos TG. Controllable fluids: the temperature dependence of post-yield properties. Int J Mod Phys B 1994;8:3015–32. https://doi.org/10.1142/S0217979294001275.
[37] Liao C. Study on Magnetorheological Fluid Damper for Automobile Suspension System. Chongqing Chong Qing Univ; 2001.
[38] Sohn JW, Jeon J, Nguyen QH, Choi S-B. Optimal design of disc-type magneto-rheological brake for mid-sized motorcycle: experimental evaluation. Smart Mater Struct 2015;24:85009. https://doi.org/10.1088/0964-1726/24/8/085009.
[39] Pilch Z. Analysis of established thermal conditions for magnetorheological clutch for different loading conditions. Springer, Cham; 2015. doi: 10.1007/978-3-319-11248-0_16.
[40] Andersen SB, Santos IF, Fuerst A. Multi-physics modeling of large ring motor for mining industry – combining electromagnetism, fluid mechanics, mass and heat transfer in engineering design. Appl Math Model 2015;39:1941–65. https://doi.org/10.1016/j.apm.2014.10.017.
[41] Bergman TL, Lavine AS, Incropera FP, DeWitt DP. Fundamentals of heat and mass transfer. 7th ed. Wiley; 2010.
[42] McAdams WH. Heat transmission. 3rd ed. McGraw-Hill; 1954.
[43] Warner Charles Y, Arpaci Vrdt S. An experimetal investigation of turbulent natural convection in air at low pressure along a vertical heated flat plate. Int J Heat Mass Transf 1968;11:397–406. https://doi.org/10.1016/0017-9310(68)90084-7.
[44] Bayley F. An analysis of turbulent free-convection heat-transfer. Proc Inst Mech 1955;169:361–70. https://doi.org/10.1243/PIME_PROC_1955_169_049_02.
[45] Churchill SW, Chu HHS. Correlating equations for laminar and turbulent free convection from a vertical plate. Int J Heat Mass Transf 1975;18:1323–9. https://doi.org/10.1016/0017-9310(75)90243-4.
[46] Lloyd JR, Moran WR. Natural convection adjacent to horizontal surface of various planforms. J Heat Transfer 1974;96:443–7. https://doi.org/10.1115/1.3450224.
[47] Radziemska E, Lewandowski WM. Heat transfer by natural convection from an isothermal downward-facing round plate in unlimited space. Appl Energy 2001;68:347–66. https://doi.org/10.1016/S0306-2619(00)00061-1.
[48] Rohsenow W, Hartnett J, Cho Y. Handbook of heat transfer. New York: McGraw-Hill; 1998.
[49] Sadiku M. Elements of Electromagnetics. USA: Oxford University Press; 1994.
[50] Edminister J. Electromagnetics. Schaum's Outline series. McGraw-Hill; 1979.
[51] Chapman SJ. Electric Machinery Fundamentals. 4th. McGraw-Hill Education; 2010.
[52] Suisse BE. Research for dynamic seal friction modeling in linear motion hydraulic piston applications; 2005.
[53] Yu J, Dong X, Wang W. Prototype and test of a novel rotary magnetorheological damper based on helical flow. Smart Mater Struct 2016;25:25006. https://doi.org/10.1088/0964-1726/25/2/025006.
[54] Jolly MR, Bender JW, Carlson JD. Properties and applications of commercial magnetorheological fluids. J Intell Mater Syst Struct 1999;10:5–13. https://doi.org/10.1177/1045389X9901000102.
[55] Phillips RW. Engineering application of fluids with a variable yield stress. Berkeley: University of California; 1969.
[56] Zhang JQ, Feng ZZ, Jing Q. Optimization analysis of a new vane MRF damper. J Phys Conf Ser 2009;149:12087. https://doi.org/10.1088/1742-6596/149/1/012087.
[57] Yang L, Chen SZ, Zhang B, Feng ZZ. A rotary magnetorheological damper for a tracked vehicle. Adv Mater Res 2011;328–330:1135–8. https://doi.org/10.4028/www.scientific.net/AMR.328-330.1135.
[58] Imaduddin F, Mazlan SA, Zamzuri H. Modeling review of rotary magnetorheological damper. J Mater 2013;51:575–91. https://doi.org/10.1016/j.matdes.2013.04.042.
[59] Millonas MM. Swarms, Phase Transitions, and Collective Intelligence (Paper 1); and A Nonequilibrium Statistical Field Theory of Swarms and Other Spatially Extended Complex Systems (Paper 2). Work Pap; 1993.
[60] Shi Y, Eberhart R. A modified particle swarm optimizer IEEE Int Conf Evol Comput Proceedings IEEE World Congr Comput Intell (Cat. No.98TH8360); 1998, p. 69–73 10.1109/ICEC.1998.699146.
[61] Bansal JC, Singh PK, Saraswat M, Verma A, Jadon SS, Abraham A. inertia weight strategies in particle swarm Third world Congr Nat Biol. inspired Comput (NaBIC 2011), IEEE, Salamanca, Spain; 2011, p. 640–7.
[62] van den Bergh F, Engelbrecht AP. A new locally convergent particle swarm optimiser. IEEE Int Conf Syst Man Cybern 2002; 3: 6 pp. doi: 10.1109/ICSMC.2002.1176018.
[63] Krink T, Vesterstrom JS, Krink RJ, Vesterstrom T, Particle swarm optimization with spatial particle extension. Proc IEEE Congr Evol Comput (CEC 2002) 2002; 2: 1474–9. 10.1109/CEC.2002.1004460.
[64] Kennedy J. Swarm Intelligence Handb Nature-Inspired Innov Comput. Boston: Kluwer Academic Publishers; 2006, p. 187–219. doi: 10.1007/0-387-27705-6_6.
[65] Eberhart R, Simpson PK, Dobbins RW. Computational Intelligence PC Tools Acad Press 1996:611–6.
[66] Nguyen P-B, Choi S-B. A new approach to magnetic circuit analysis and its application to the optimal design of a bi-directional magnetorheological brake. Smart Mater Struct 2011;20:125003. https://doi.org/10.1088/0964-1726/20/12/125003.
[67] Chootinan P, Chen A. Constraint handling in genetic algorithms using a gradient-based repair method. Comput Oper Res 2006;33:2263–81. https://doi.org/10.1016/j.cor.2005.02.002.
[68] Campbell SL, Meyer CD. Generalized Inverses of Linear Transformations. vol. 56. Society for industrial and Applied Mathematics; 1979. doi: 10.1137/1.9780898719048.
[69] Wang Y, Li B, Weise T, Wang J, Yuan B, Tian Q. Self-adaptive learning based particle swarm optimization. Inf Sci (Ny) 2011;181:4515–38. https://doi.org/10.1016/j.ins.2010.07.013.
[70] Monson CK, Seppi KD. Exposing origin-seeking bias in PSO. Proc 2005 Conf Genet Evol Comput – GECCO '05; 2005: 241. doi: 10.1145/1068009.1068045.

**Okan Topçu** obtained his B.Sc. in Mechanical Engineering from Kirikkale University, Turkey. He received M.Sc. in Mechanical Engineering from TOBB University of Economics and Technology, where he is currently a Ph.D. candidate. His research focuses on particle swarm optimization and rotary magnetorheological fluid devices. Okan Topçu is a graduate student member of ASME, IEEE, AIAA, and IAENG.

**Yiğit Taşcıoğlu** received his B.S. in Mechanical Engineering from Middle East Technical University, M.Sc. and Ph.D. in Mechatronics from Loughborough University. Since 2006, he is with the Mechanical Engineering Department, TOBB University of Economics and Technology. He is also the founding coordinator of the Mechatronics Minor Program.

**E. İlhan Konukseven** obtained Ph.D. degree in Mechanical Engineering from METU. During his Post-Doc studies he has focused on mobile robotics and sensor based motion planning at Mechanical Engineering Department, Carnegie Mellon University. His research interests focus on robotics, robotic machining & deburring, virtual reality, haptic devices, sensor based motion planning and mobile robotics.